The Tellurophosphate $K_4P_8Te_4$: Phase-Change Properties, Exfoliation, Photoluminescence in Solution and Nanospheres

In Chung,[†,‡] Jung-Hwan Song,[§] Myung Gil Kim,[‡] Christos D. Malliakas,[†,‡] Angela L. Karst,[†] Arthur J. Freeman,[§] David P. Weliky,[†] and Mercouri G. Kanatzidis*[‡]

Department of Chemistry, Michigan State University, East Lansing, Michigan 48824, and Department of Chemistry and Department of Physics and Astronomy, Northwestern University, Evanston, Illinois 60208

Received August 27, 2009; E-mail: m-kanatzidis@northwestern.edu

Abstract: We describe the inorganic polymer $K_4P_8Te_4$ which is soluble, giving solutions that exhibit white emission upon 355 nm laser irradiation. An indirect band gap semiconductor ($E_g \approx 1.4$ eV), $K_4P_8Te_4$ crystallizes in the space group $P2_1/m$, with $a = 6.946(1)$ Å, $b = 6.555(1)$ Å, $c = 9.955(2)$ Å, and $\beta = 90.420(3)°$ at 173(2) K. The compound features infinite chains of $[P_8Te_4{}^{4-}]$ with covalent P−Te bonding and exhibits reversible crystal−glass phase-change behavior. When deposited from solution, the material forms highly crystalline $K_4P_8Te_4$ nanospheres. The thermal analysis, FT-IR, UV−vis diffuse reflectance, ^{31}P magic angle spinning solid-state NMR spectroscopy, and pair distribution function (PDF) analysis for the crystal and glass forms and *ab initio* electronic structure calculations by the screened-exchange local density function approximation are also reported. Speciation of $K_4P_8Te_4$ in solution studied with ^{31}P solution-state NMR spectroscopy, electrospray ionization mass spectrometry, and PDF analysis indicate exfoliation of $[P_8Te_4{}^{4-}]$ chains followed by rearrangement into molecular species.

1. Introduction

Solid-state compounds with P−Te bonding have long been elusive, although phosphorus, in general, has been known to combine with nearly all elements.[1] The paucity of P−Te bonds is in striking contrast to the well-established metal chalcophosphate class[2−6] involving the ternary (M/P/Q) and quaternary (A/M/P/Q) compounds with $[P_xQ_y]^{z-}$ anions. The only reported P/Te containing inorganic compounds are MPTe (M = Ru, Os,[7] Ir[8]) and BaP_4Te_2.[9] The latter features P−Te bonding, while only unit cell dimensions and spectroscopic data have been reported for the former. On the other hand, organometallic compounds provide some examples of P−Te bonded species, for example, Et_3PTeX_2 (X = Cl, Br, I),[10] $TePPh_2Ch_3$[11] and $Ph_3PTe(Ph)I$.[12]

The larger elements in group 15, As, Sb, and Bi, show a wealth of chemistry with Te to produce a broad set of solid-state inorganic materials.[13−15]

Recently, we reported rational synthesis conditions that stabilize P-rich species and avoid the simple classical $[PSe_4]^{3-}$ and $[P_2Se_6]^{4-}$ anions through the use of excess phosphorus in the flux. Examples are $A_6P_8Se_{18}$ (A = K, Rb, Cs),[16] $Rb_4P_6Se_{12}$,[17] $Cs_4P_6Se_{12}$, and $Cs_5P_5Se_{12}$,[18] yet with the exception of BaP_4Te_2 there is a scarcity of species with P−Te bonds.

Here we report on the new alkali tellurophosphate compound $K_4P_8Te_4$ featuring P−Te bonding and the infinite anion $[P_8Te_4{}^{4-}]$. The compound was prepared with the molten salt flux method[2,19] at intermediate temperature, and it shows reversible phase-change behavior. $K_4P_8Te_4$ was found to be soluble in hydrazine to give a colloidal solution of $_n^1[P_8Te_4{}^{4-}]$ species. This is a useful property of $K_4P_8Te_4$, because, generally, it is very difficult to disperse polymeric solids in polar solvents.

† Michigan State University.
‡ Department of Chemistry, Northwestern University.
§ Department of Physics and Astronomy, Northwestern University.

(1) von Schnering, H. G.; Hönle, W. *Chem. Rev.* **1988**, *88*, 243–273.
(2) Chondroudis, K.; Hanko, J. A.; Kanatzidis, M. G. *Inorg. Chem.* **1997**, *36*, 2623–2632.
(3) Chondroudis, K.; McCarthy, T. J.; Kanatzidis, M. G. *Inorg. Chem.* **1996**, *35*, 840–844.
(4) Mccarthy, T. J.; Kanatzidis, M. G. *Inorg. Chem.* **1995**, *34*, 1257–1267.
(5) Chondroudis, K.; Kanatzidis, M. G. *Inorg. Chem.* **1995**, *34*, 5401–5402.
(6) Mccarthy, T. J.; Kanatzidis, M. G. *Chem. Mater.* **1993**, *5*, 1061–1063.
(7) Lutz, H. D.; Schmidt, T.; Waschenbach, G. *Z. Anorg. Allg. Chem.* **1988**, *562*, 7–16.
(8) Kliche, G. *Z. Naturforsch., B* **1986**, *41*, 130–131.
(9) Jörgens, S.; Johrendt, D.; Mewis, A. *Chem.−Eur. J.* **2003**, *9*, 2405–2410.
(10) Konu, J.; Chivers, T. *Dalton Trans.* **2006**, 3941–3946.
(11) Dornhaus, F.; Bolte, M.; Lerner, H. W.; Wagner, M. *Eur. J. Inorg. Chem.* **2006**, 1777–1785.

(12) Boyle, P. D.; Cross, W. I.; Godfrey, S. M.; McAuliffe, C. A.; Pritchard, R. G.; Sarwar, S.; Sheffield, J. M. *Angew. Chem., Int. Ed.* **2000**, *39*, 1796–1798.
(13) Poudeu, P. F. P.; Kanatzidis, M. G. *Chem. Commun.* **2005**, 2672–2674.
(14) Hsu, K. F.; Lal, S.; Hogan, T.; Kanatzidis, M. G. *Chem. Commun.* **2002**, 1380–1381.
(15) Sheldrick, W. S.; Wachhold, M. *Coord. Chem. Rev.* **1998**, *176*, 211–322.
(16) Chondroudis, K.; Kanatzidis, M. G. *Inorg. Chem.* **1998**, *37*, 2582–2584.
(17) Chung, I.; Karst, A. L.; Weliky, D. P.; Kanatzidis, M. G. *Inorg. Chem.* **2006**, *45*, 2785–2787.
(18) Chung, I.; Jang, J. I.; Gave, M. A.; Weliky, D. P.; Kanatzidis, M. G. *Chem. Commun.* **2007**, 4998–5000.
(19) Kanatzidis, M. G. *Curr. Opin. Solid State Mater. Sci.* **1997**, *2*, 139–149.

As a result, little is known about the behavior of inorganic polymers in solution. In some cases, these solutions have shown interesting mesogenic liquid crystal properties, for example, $[V_{0.837}P_2S_6^-]$,[20] $\frac{1}{\infty}[CrP_2S_6^-]$,[21] $\frac{1}{\infty}[PdPS_4^-]$[22,23] and $\frac{1}{\infty}[Mo_3Se_3^-]$.[24−27] The possibility to exfoliate or even dissolve mineral compounds is of major importance because it can allow for patterned deposition and modification of the structure with solution chemistry methods paving the way to new organic−inorganic hybrid and nanocomposite materials. The solutions of $K_4P_8Te_4$ exhibit slightly blue-tinted white photoluminescence at room temperature when excited above the energy gap. Precipitation with ethanol at room temperature gave nanospheres of $K_4P_8Te_4$ exhibiting a blue-shifted energy band gap. With a wide battery of spectroscopic techniques, we show that in solution $K_4P_8Te_4$ exfoliates and with time the $[P_8Te_4^{4-}]$ chains rearrange to small molecular species. We also describe the results of ab initio density functional theory calculations using the all-electron full-potential linearized augmented plane wave (FLAPW)[28] method, which show that $K_4P_8Te_4$ is an indirect band gap semiconductor and has a strong covalent bonding character of P−Te.

2. Experimental Section

2.1. Reagents. The reagents mentioned in this work were used as obtained unless noted otherwise: K metal (analytical reagent, Aldrich Chemical Co., Milwaukee, WI); red phosphorus powder (99%, Sigma-Aldrich Inc., Saint Louis, MO); Te (99.999%, Noranda Advanced Materials, Quebec, Canada); *N,N*-dimethylformamide (ACS reagent grade, Spectrum Chemicals,); diethyl ether (anhydrous, ACS reagent grade, Columbus Chemical Industries, Columbus, WI,); hydrazine (98%, anhydrous, Sigma-Aldrich Inc., Saint Louis, MO). K_2Te starting material was prepared by reacting stoichiometric amounts of the elements in liquid ammonia. Anhydrous hydrazine was distilled before use. **CAUTION: Hydrazine is highly toxic and should be handled using proper protective equipments with special care to prevent contact with either the vapors or liquid.**

2.2. Synthesis. All sample preparation processes were carried out under inert atmosphere. Pure $K_4P_8Te_4$ was achieved by heating a mixture of $K_2Te/P/Te = 3:2:5$ under vacuum in a silica tube at 450 °C for 6 days, followed by cooling to 250 at 2 °C h^{-1}. The excess flux was dissolved with degassed *N,N*-dimethylformamide (DMF) under a N_2 atmosphere to reveal deep red-tinted black needle crystals. Energy-dispersive spectroscopy microprobe analysis on five crystals showed an average composition of "$K_{3.8}P_8Te_{3.7}$". The single crystals appear stable in DMF, *N*-methylformamide, deionized H_2O, and air. Attempts to synthesize other alkali metal analogues with similar reaction conditions were unsuccessful.

2.3. Physical Measurements. 2.3.1. X-ray Powder Diffraction. X-ray powder diffraction analyses were performed using a calibrated CPS 120 INEL X-ray powder diffractometer (Cu Kα graphite monochromatized radiation) operating at 40 kV/20 mA and equipped with a position-sensitive detector with flat sample geometry.

2.3.2. Scanning Electron Microscopy. Semiquantitative analyses of the compound was performed with a JEOL JSM-35C scanning electron microscope (SEM) equipped with a Tracor Northern energy dispersive spectroscopy (EDS) detector.

2.3.3. Transmission Electron Microscopy (TEM) and High Resolution (HR) TEM. TEM sample was diluted with ethanol. TEM and HRTEM images were obtained with JEOL JEM 2200 FS Field emission TEM.

2.3.4. Solid-state UV−vis Spectroscopy. Optical diffuse reflectance measurements were performed at room temperature using a Shimadzu UV-3101 PC double-beam, double-monochromator spectrophotometer operating in the 200−2500 nm region. The details of the energy gap measurements have been discussed elsewhere.[29−33]

2.3.5. Infrared Spectroscopy. FT-IR spectrum was recorded as a solid in a CsI matrix. The sample was ground with dry CsI into a fine powder and pressed into a translucent pellet. The spectrum was recorded in the far-IR region (600−100 cm^{-1}, 4 cm^{-1} resolution) with the use of a Nicolet 740 FT-IR spectrometer equipped with a TGS/PE detector and silicon beam splitter.

2.3.6. Thermogravimetric Analysis. Experiments were performed on Shimadzu TGA-50 thermal analyzer by heating the samples up to 500 °C at a rate of 10 °C min^{-1} under N_2 flow of ca. 20 mL min^{-1}.

2.3.7. Differential Thermal Analysis (DTA). Experiments were performed on Shimadzu DTA-50 thermal analyzer. A sample ($\sim$30 mg) of ground crystalline material was sealed in a silica ampule under vacuum. A similar ampule of equal mass filled with Al_2O_3 was sealed and placed on the reference side of the detector. The sample was heated to 550 at 5 °C min^{-1}, and after 1 min it was cooled at a rate of −5 °C min^{-1} to 50 °C. The residues of the DTA experiments were examined by X-ray powder diffraction. Reproducibility of the results was confirmed by running multiple heating/cooling cycles. The melting and crystallization points were measured at a minimum of endothermic peak and a maximum of exothermic peak.

2.3.8. ^{31}P Solid-State NMR Spectroscopy. Room temperature ^{31}P NMR measurements were taken on a 9.4 T 400 MHz Varian Infinity Plus NMR spectrometer using a double-resonance magic angle spinning (MAS) probe using a 4 mm (outer) diameter zirconia rotor. Bloch decay spectra were taken with the excitation/detection channel tuned to ^{31}P at 161.82 MHz with a 4.5 μs, 90° pulse (calibrated to ±0.5 μs), a relaxation delay of 20−13000 s, and samples were spun at frequencies between 6 and 13 kHz. All spectra were processed with up to 100 Hz of line broadening, up to a tenth-order polynomial baseline correction, and the chemical shifts (CS) were externally referenced to 85% H_3PO_4 at 0 ppm. The spin−lattice relaxation time (T_1) of each chemical shift was estimated from the exponential buildup of the peak intensity area as a function of the relaxation delay at 13 kHz between 20 and 13000 s. The chemical shift anisotropy (CSA) principle value of each chemical shift was derived from the average of the Herzfeld−Berger fitting[34] of the MAS isotropic and sideband peak intensity areas at spinning

(20) Coste, S.; Gautier, E.; Evain, M.; Bujoli-Doeuff, M.; Brec, R.; Jobic, S.; Kanatzidis, M. G. *Chem. Mater.* **2003**, *15*, 2323−2327.

(21) Coste, S.; Kopnin, E.; Evain, M.; Jobic, S.; Brec, R.; Chondroudis, K.; Kanatzidis, M. G. *Solid State Sci.* **2002**, *4*, 709−716.

(22) Sayettat, J.; Bull, L. M.; Jobic, S.; Gabriel, J. C. P.; Fourmigue, M.; Batail, P.; Brec, R.; Inglebert, R. L.; Sourisseau, C. *J. Mater. Chem.* **1999**, *9*, 143−153.

(23) Sayettat, J.; Bull, L. M.; Gabriel, J. C. P.; Jobic, S.; Camerel, F.; Marie, A. M.; Fourmigue, M.; Batail, P.; Brec, R.; Inglebert, R. L. *Angew. Chem., Int. Ed.* **1998**, *37*, 1711−1714.

(24) Song, J. H.; Messer, B.; Wu, Y. Y.; Kind, H.; Yang, P. D. *J. Am. Chem. Soc.* **2001**, *123*, 9714−9715.

(25) Venkataraman, L.; Lieber, C. M. *Phys. Rev. Lett.* **1999**, *83*, 5334−5337.

(26) Davidson, P.; Gabriel, J. C.; Levelut, A. M.; Batail, P. *Europhys. Lett.* **1993**, *21*, 317−322.

(27) Tarascon, J. M.; Disalvo, F. J.; Chen, C. H.; Carroll, P. J.; Walsh, M.; Rupp, L. *J. Solid State Chem.* **1985**, *58*, 290−300.

(28) Wimmer, E.; Krakauer, H.; Weinert, M.; Freeman, A. J. *Phys. Rev. B* **1981**, *24*, 864−875.

(29) Wendlandt, W. W.; Hecht, H. G. *Reflectance Spectroscopy*; Interscience Publishers: New York, 1966.

(30) Kortüm, G. *Reflectance Spectroscopy. Principles, Methods, Applications*; Springer: New York, 1969.

(31) Tandon, S. P.; Gupta, J. P. *Phys. Status Solidi* **1970**, *38*, 363−367.

(32) Chung, D. Y.; Choi, K. S.; Iordanidis, L.; Schindler, J. L.; Brazis, P. W.; Kannewurf, C. R.; Chen, B. X.; Hu, S. Q.; Uher, C.; Kanatzidis, M. G. *Chem. Mater.* **1997**, *9*, 3060−3071.

(33) Stephan, H. O.; Kanatzidis, M. G. *Inorg. Chem.* **1997**, *36*, 6050−6057.

(34) Herzfeld, J.; Berger, A. E. *J. Chem. Phys.* **1980**, *73*, 6021−6030.

Table 1. Crystallographic Refinement Details for K$_4$P$_8$Te$_4$

formula	K$_4$P$_8$Te$_4$
crystal system, space group	monoclinic $P2_1/m$ (No. 11)
unit cell dimensions,	$a = 6.946(1)$ Å, $b = 6.555(1)$ Å,
	$c = 9.955(2)$ Å, $\beta = 90.420(3)°$
Z	1
V, Å^3	453.2(2)
d (calculated), g cm^{-3}	3.351
crystal dimensions, mm^3	$0.114 \times 0.010 \times 0.008$
temperature, K	173(2)
λ, Å	0.71073
μ, mm^{-1}	7.969
$F(000)$	404
θ_{max}, deg	28.30
total/unique reflections	4713/1167
R_{int}	0.0443
no. parameters	46
refinement method	Full-matrix least-squares on F^2
final R indices [$I > 2\sigma(I)$], $R_1{}^a/wR_2{}^b$	0.0397/0.0889
R indices (all data), R_1/wR_2	0.0560/0.0958
goodness-of-fit on F^2	1.099

$^a R_1 = \sum ||F_o| - |F_c||/\sum|F_o|.$ $^b wR_2 = \{\sum [w(F_o{}^2 - F_c{}^2)^2]/\sum[w(F_o{}^2)^2]\}^{1/2}.$

frequencies of 8, 8.5, and 10 kHz for the peak at −4.3 ppm, at 6, 8, 8.5, 10, and 12 kHz for the peak at −16.9 ppm, and at 8, 8.5, 10, 12, and 13 kHz for the peak at −34.6 ppm (outliers were excluded).

2.3.9. ^{31}P Solution-State NMR Spectroscopy and Electrospray Ionization (ESI) Mass Spectrometry. Room temperature ^{31}P NMR measurements were taken on a 400 MHz Varian INOVA NMR spectrometer. The chemical shifts were externally referenced to 85% H$_3$PO$_4$ at 0 ppm. ESI mass spectroscopic measurements were performed with Agilent MSD 1100 high performance liquid chromatography system. ^{31}P solution-state NMR spectra were taken right after ESI mass spectra measurements with the same solution.

2.3.10. X-ray Crystallography. The crystal structure was determined by single-crystal X-ray diffraction methods. Preliminary examination and data collection were performed on a SMART[35] platform diffractometer equipped with a 1K CCD area detector using graphite monochromatized Mo Kα radiation at 173(2) K. A full sphere of data was collected at 173(2) K using the narrow-frame method with scan widths of 0.30° in ω and exposure time of 50 s frame^{-1}. The SAINT software was used for data extraction and integration. Semiempirical absorption correction using the program SADABS was performed. The initial positions for all atoms were obtained using direct methods, and the structure was refined with the full-matrix least-squares techniques of the SHELXTL crystallographic software package. Satisfactory refinement was obtained with the centrosymmetric $P2_1/m$. All atoms were refined to full occupancy and anisotropically. ADDSYM from the PLATON program[36] was used for checking out higher symmetry. The parameters for data collection, details of the structural refinement, and fractional atomic coordinates and displacement parameters are given in Tables 1 and 2.

2.3.11. Atomic Pair Distribution Function Analysis. Fine powders (<40 μm) of the crystalline and glassy K$_4$P$_8$Te$_4$ were packed in a Kapton capillary with a 1.0 mm diameter. Diffraction data were collected at room temperature using the rapid acquisition pair distribution function technique.[37] Data were also collected using an MAR345 image plate detector and ∼ 60 keV energy X-rays (λ = 0.2128 Å) at the 11-ID-B beamline at the Advanced Photon Source. Measurements were repeated 4−5 times per sample to improve counting statistics. The data were combined and inte-

Table 2. Atomic Coordinates ($\times 10^4$) and Equivalent Isotropic Displacement Parameters (Å^2 $\times 10^3$) for K$_4$P$_8$Te$_4$ at 173(2) K. U_{eq} is Defined As One Third of the Trace of the Orthogonalized U_{ij} Tensor

	x	y	z	U_{eq}
K(1)	261(3)	2500	3890(2)	18(1)
K(2)	2211(3)	2500	68(2)	19(1)
P(1)	3906(2)	52(3)	5802(2)	10(1)
P(2)	4918(4)	2500	2978(3)	10(1)
P(3)	4927(4)	2500	7169(3)	11(1)
Te(1)	7054(1)	2500	1014(1)	13(1)
Te(2)	8481(1)	2500	7335(1)	15(1)

grated using the program FIT2D.[38] Various corrections were made to the data, such as subtraction of background, Compton and fluorescence scattering, geometric corrections, absorption, and so on, as described previously.[39,40] Corrections were made using the program PDFgetX2.[41] The structural model was fit to the data using the program PDFFIT.[42]

3. Results and Discussion

3.1. Crystal Structure. K$_4$P$_8$Te$_4$ adopts the $P2_1/m$ space group and features parallel infinite one-dimensional straight chains of [P$_8$Te$_4{}^{4-}$], Figure 1. This anion is unique in that it has no reported sulfur or selenium analogue. The only other compound which features this species is the orthorhombic BaP$_4$Te$_2$. Because of the different number and size of the counter-cations of K$^+$ and Ba^{2+} in the lattice, the chains adopt different crystal packing. The P$_8$ backbone of the chain is made of six-membered P$_6$-rings in a cyclohexane-like chair conformation which are equatorially condensed via opposite edges of the hexagon defined by the P(1) atoms. This creates 3-coordinate P atoms. The equatorial and axial Te(1) and Te(2) atoms are bonded to P(2) and P(3) with distances of 2.463(3) and 2.472(3) Å, respectively. This is comparable to the sum of covalent radii at 2.47 Å.[43] The P−Te bonds in organometallic compounds are also similar, for example, 2.473(1) Å in Et$_3$PTeBr$_2$.[10] The dihedral angles of P(3)−P(1)−P(1)−P(3) and P(3)−P(1)···P(2)−P(1) in the [P$_8$Te$_4{}^{4-}$] chain are −180.0(1)° and −1.8(1)°, respectively, indicating that the P$_8$ backbone chain is nearly ideal. The P−P distances at 2.214(3), 2,217(2), and 2.220(2) Å are comparable to those found in low valent chalcophosphate compounds.[16−18]

Interchain Te···Te nonbonding interactions, which are shorter than the sum of van der Waals radii of 4.40 Å,[44] are observed for Te(1)···Te(2) at 3.8016(7) Å (see Figure 1b,c). This weak interaction helps to organize the [P$_8$Te$_4{}^{4-}$] chains arranged side by side to form layers. The K(1) atom, sandwiched by the [P$_8$Te$_4{}^{4-}$] chains, coordinates to six P and four Te atoms, whereas the K(2) atom, residing at the corner of four [P$_8$Te$_4{}^{4-}$] chains, interacts to two P and five Te atoms in a distorted pentagonal bipyramidal geometry (Figure 2a,b). The distances

(35) *SADABS, SHELXTL*, version 6; Bruker Analytical X-ray Instrumentals, Inc.: Madison, WI, 2000.

(36) Spek, A. L. *J. Appl. Crystallogr.* **2003**, *36*, 7–13.

(37) Chupas, P. J.; Qiu, X. Y.; Hanson, J. C.; Lee, P. L.; Grey, C. P.; Billinge, S. J. L. *J. Appl. Crystallogr.* **2003**, *36*, 1342–1347.

(38) Hammersley, A. P.; Svensson, S. O.; Hanfland, M.; Fitch, A. N.; Hausermann, D. *High Pressure Res.* **1996**, *14*, 235–248.

(39) Kim, H.; Malliakas, C.; Tomic, A.; Tessmer, S.; Kanatzidis, M.; Billinge, S. *Phys. Rev. Lett.* **2006**, *96*, 226401.

(40) Egami, T.; Billinge, S. J. L. *Underneath the Bragg Peaks: Structural Analysis of Complex Materials*, 1st ed.; Pergamon: Amsterdam; Boston, 2003.

(41) Qiu, X. Y.; Bozin, E. S.; Juhas, P.; Proffen, T.; Billinge, S. J. L. *J. Appl. Crystallogr.* **2004**, *37*, 110–116.

(42) Proffen, T.; Billinge, S. J. L. *J. Appl. Crystallogr.* **1999**, *32*, 572–575.

(43) Pauling, L. *The Nature of the Chemical Bond and the Structure of Molecules and Crystals; An Introduction to Modern Structural Chemistry*, 3d ed.; Cornell University Press: Ithaca, NY, 1960.

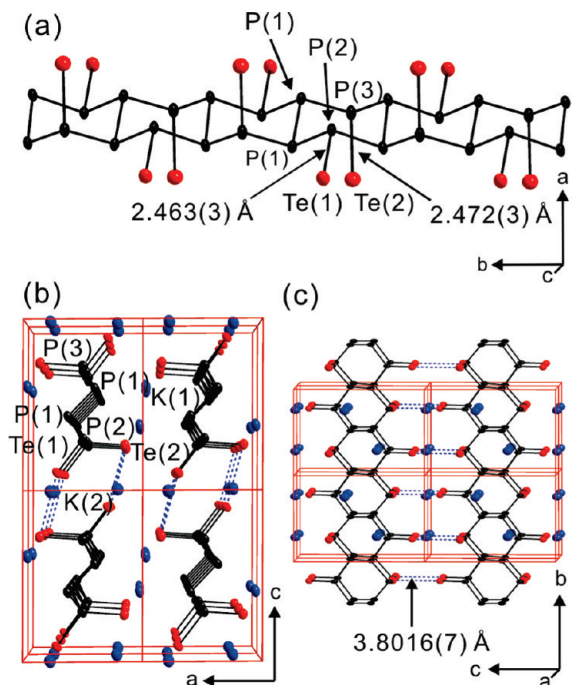(44) Cherin, P.; Unger, P. *Acta Crystallogr.* **1967**, *23*, 670–671.

Figure 1. (a) View of a segment of a $\frac{1}{\infty}[P_8Te_4^{4-}]$ chain. P and Te atoms are labeled. (b) Structure of $K_4P_8Te_4$ viewed down the chain direction, *b*-axis. (c) View down the *a*-axis. Dashed line denotes short Te⋯Te interaction at Te(1)⋯Te(2), 3.8016(7) Å. Blue circles represent K atoms. The thermal ellipsoids are shown with 90% in panel a and 50% probability in panels b and c.

of K to P atoms range from 3.359(3) to 3.814(3) Å, and those to Te atoms are at 3.487(2) to 3.744(3) Å, Table 3. Note that the atoms K(1)−Te(1)−K(2)−P(2) are coplanar and the distance of K(1)⋯K(2) is 4.0483(7) Å (Figure 2c).

3.2. Thermal Analysis and Spectroscopy. Differential thermal analysis (DTA) of $K_4P_8Te_4$, performed in a closed container at a rate of 5 °C min^{-1}, showed melting at 488 °C. Upon cooling, the melt formed a black glass (Figure 3a). On subsequent heating, the glass recrystallized at 455 °C and again melted at 488 °C to form a glass upon cooling. The amorphous nature of the glassy phase was confirmed with X-ray powder diffraction. The powder diffraction pattern after recrystallization at 455 °C was identical to that of pristine $K_4P_8Te_4$ indicating full recovery of the original crystal structure (Figure 3b). The reversible crystal-glass transition was repeatedly observed in multiple DTA cycles, indicating congruent melting of the substance.

Thermogravimetric analysis (TGA) at a rate of 10 °C min^{-1} (open container) showed that the compound decomposed under N_2 flowing from ∼300 to 430 °C with a weight loss of 27.3%. This value is in excellent agreement with the theoretical P content in the compound of 27.09% and suggested that the polyphosphorus backbone was destroyed by heating at >300 °C. X-ray powder patterns of the black residue after TGA revealed a mixture of α-K_2Te_2, K_2Te_3, and K_5Te_3 along with a small amount of amorphous phase. The DTA and TGA results suggest that above the melting point the following equilibrium is in effect:

$$K_4P_8Te_4 \rightleftharpoons 2K_2Te_2 + 2P_4\uparrow \qquad (1)$$
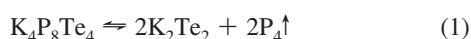
The solid-state UV−vis absorption spectra of the crystalline and glassy phases show absorption edges at 1.40 and 0.91 eV, respectively, Figure 3c. The lower energy gaps of the glass can be attributed to structural defects that create midgap states and
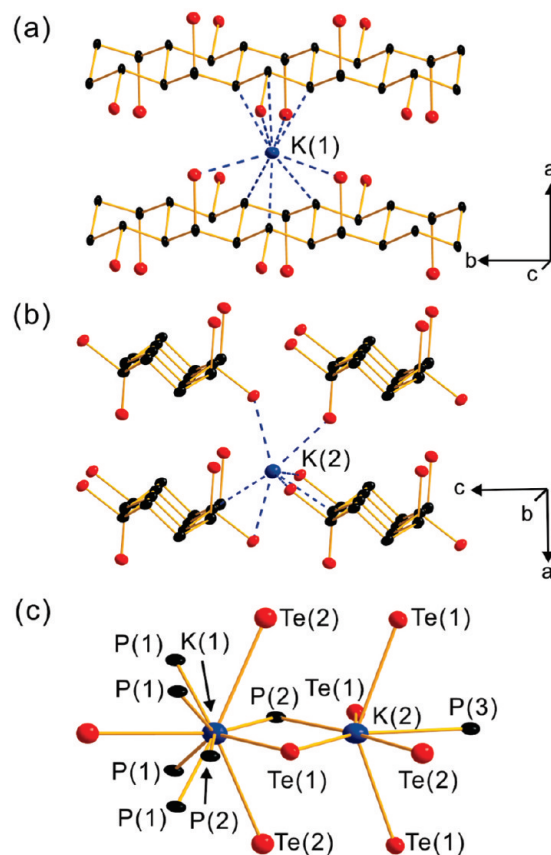

Figure 2. Local coordination environment of K(1) and K(2) atoms. (a) K(1) atom sandwiched by two $\frac{1}{\infty}[P_8Te_4^{4-}]$ chains and (b) K(2) atom surrounded by four $[P_8Te_4^{4-}]$ chains are shown. Blue broken line denotes ionic bonding of K atoms to P and Te atoms in panels a and b. (c) K(1) and K(2) dimer is shown with K, P, and Te atoms labeled. Thermal ellipsoids are shown with 90% probability.

Table 3. Selected Bond Distances (Å) and Angles (deg) for $K_4P_8Te_4$ at 173(2) K[a]

P(1)−P(1)	2.214(3)	K(2)−P(2)	3.442(3)
P(1)−P(2)	2.220(2) × 3	K(2)−P(3)[vii]	3.460(4)
P(1)−P(3)	2.217(2) × 2	K(2)−Te(1)	3.487(2)
P(2)−Te(1)	2.463(3)	K(2)−Te(1)[viii]	3.489(1)
P(3)−Te(2)	2.472(3)	K(2)−Te(1)[xi]	3.488(1)
		K(2)−P(1)[iv]	3.710(3)
K(1)−P(1)	3.541(3)	K(2)−P(2)[x]	3.744(3)
K(1)−P(1)[i,ii]	3.359(3)		
K(1)−P(1)[iii]	3.541(3)	P(1)[v]−P(1)−P(2)[v]	96.86(12)
K(1)−P(2)	3.366(3)	P(1)[v]−P(1)−P(3)	104.29(13)
K(1)−P(2)[iv]	3.814(3)	P(1)[iii]−P(3)−P(2)	92.72(13)
K(1)−Te(1)[iv]	3.615(3)	P(3)−P(1)−P(2)[v]	95.44(9)
K(1)−Te(2)[v,vi]	3.607(1)	P(1)[v]−P(2)−Te(1)	102.29(9)
K(1)−Te(2)[iv]	3.653(3)	P(1)−P(3)−Te(2)	110.84(9)

[a] Symmetry transformations used to generate equivalent atoms: (i) −x, y + 1/2, −z + 1; (ii) −x, −y, −z + 1; (iii) x, −y + 1/2, z; (iv) x − 1, y, z; (v) −x + 1, −y, −z + 1; (vi) −x + 1, −y + 1, −z + 1; (vii) x, y, z − 1; (viii) −x + 1, −y, −z; (ix) −x + 1, −y + 1, −z; (x) x − 1, y, z − 1; (xi) −x, −y + 1, −z + 1; (xii) −x, −y, −z.

band tailing.[45,46] The band gap value is consistent with the black color of the materials. The far-infrared spectrum displays absorption peaks at 262(w), 306(s), 322(m), 417(m), 431(s), and 469(m) cm^{-1}. The peaks at 417 and 431 cm^{-1} can be

(45) Marking, G. A.; Hanko, J. A.; Kanatzidis, M. G. *Chem. Mater.* **1998**, *10*, 1191–1199.

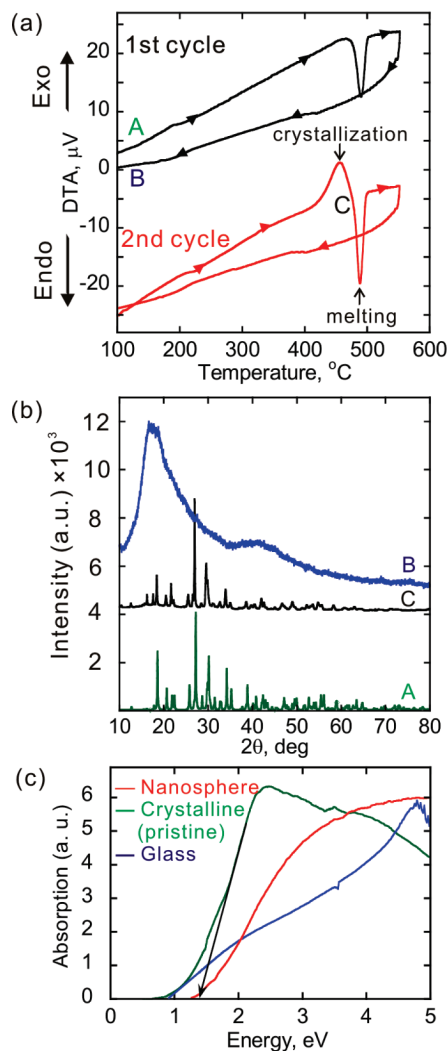(46) Dhingra, S.; Kanatzidis, M. G. *Science* **1992**, *258*, 1769–1772.

Figure 3. (a) DTA diagrams of $K_4P_8Te_4$ showing melting in the first heating cycle with no crystallization on cooling (upper black line), performed at a rate of 5 °C min^{-1}. Glass crystallization is observed in the second heating cycle (lower red line). $K_4P_8Te_4$ is a pristine crystal at A, glass at B, and restored crystal at C. (b) X-ray powder diffraction patterns of (A) theoretically simulated, (B) glass, and (C) recrystallized material. See Figure 7e for (*hkl*) indexing. (c) UV−vis absorption spectra of glass (blue), pristine crystal (green), and precipitated nanospheres (red).

assigned to P−Te by analogy to MPTe (M = Ru, Os),[7] and those at 323 and 469 cm^{-1} to a P−P vibration in comparison to Ba_3P_{14}.[47]

To probe the local structure of both the crystalline and glassy $K_4P_8Te_4$, we performed atomic pair distribution function (PDF) analysis. This technique analyzes both Bragg and diffuse scattering to reveal the short and intermediate range order of a solid regardless of the degree of disorder. Peaks in the PDF directly represent the quantitative real-space interatomic distance correlation of pairs of atoms in the structure. Thus, the technique is a powerful analytical tool for studying disorder in crystalline and amorphous phases.[48−50] The experimental PDF of crystal-
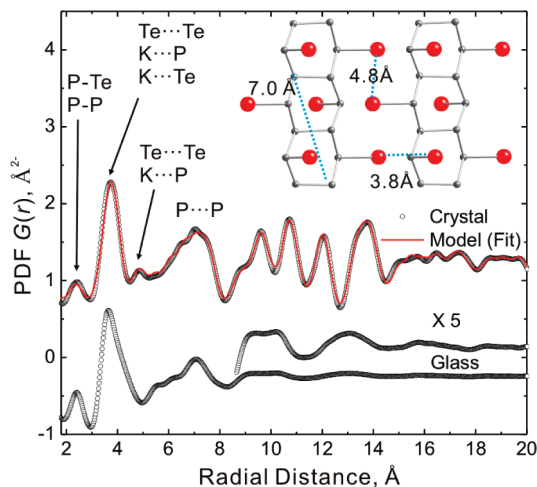

Figure 4. Experimental pair distribution function $G(r)$ of the crystalline (upper) and glassy (bottom) $K_4P_8Te_4$. The calculated PDF using the crystallographic coordinates is shown as a red line. Selected atomic correlation distances are indicated. Relevant atomic distances in the crystallographic model are also shown (inset).

line $K_4P_8Te_4$ is in excellent agreement with the calculated PDF based upon the crystallographically refined crystal structure model, validating the correctness of the crystal structure (Figure 4). The first strong correlation in the $G(r)$ at 2.4 Å is assigned to the P−P and P−Te covalent bonds in the one-dimensional chain. The second peak at 3.7 Å corresponds to the distance of short Te···Te nonbonding interchain contact and that from the K atom to the first neighboring P and Te atoms, defining the connectedness of $[P_8Te_4^{4-}]$ chain to the K atom and the nearest chain. The third peak at 4.8 Å relates the second neighboring interchain Te···Te and K···P correlations. The peak at 7.0 Å results from the P···P distances from two neighboring P hexagons.

The experimental PDF of the glass phase shows well-defined correlations but up to ∼14 Å. The first two at ∼2.4 and 3.7 Å and the broad feature at 7 Å are very similar to those in the crystalline form. Note that the peak at 7 Å defines the relation of two neighboring P hexagons in the backbone. Beyond ∼14 Å all correlations are lost, reflecting the lack of long-range periodicity. The structural coherence is much shorter than the crystalline phase but significantly longer than those of the conventional chalcogenide glasses or silica.[51,52] The PDF data suggest that the crystalline and glassy phases of $K_4P_8Te_4$ are structurally similar with respect to their local structure which is defined by a relatively large and invariant fragment. This similarity indicates the rigidity of the local structural unit $[P_8Te_4^{4-}]$, which appears to be relatively intact in the glassy form.

$K_4P_8Te_4$ is a member of a new growing class of phase change materials[18,48,49,53,54] with stoichiometric composition and mixed ionic/covalent bonding in the structure. The vast majority of chalcogenide glasses have nearly continuous compositions and

(47) Dahlmann, W.; von Schnering, H. G. *Naturwissenschaften* **1973**, *60*, 429–429.
(48) Chung, I.; Malliakas, C. D.; Jang, J. I.; Canlas, C. G.; Weliky, D. P.; Kanatzidis, M. G. *J. Am. Chem. Soc.* **2007**, *129*, 14996–15006.
(49) Wachter, J. B.; Chrissafis, K.; Petkov, V.; Malliakas, C. D.; Bilc, D.; Kyratsi, T.; Paraskevopoulos, K. M.; Mahanti, S. D.; Torbrugge, T.; Eckert, H.; Kanatzidis, M. G. *J. Solid State Chem.* **2007**, *180*, 420–431.
(50) Billinge, S. J. L.; Kanatzidis, M. G. *Chem. Commun.* **2004**, 749–760.
(51) Dejus, R. J.; Susman, S.; Volin, K. J.; Montague, D. G.; Price, D. L. *J. Non-Cryst. Solids* **1992**, *143*, 162–180.
(52) Salmon, P. S.; Petri, I. In *Workshop on Atomic Structure and Transport in Glassy Networks* Lyon, France, 2002, p S1509−S1528.
(53) Chung, I.; Do, J.; Canlas, C. G.; Weliky, D. P.; Kanatzidis, M. G. *Inorg. Chem.* **2004**, *43*, 2762–2764.
(54) Kaidatzis, A.; Wachter, J. B.; Chrissafis, K.; Paraskevopoulos, K. M.; Kanatzidis, M. G. *J. Non-Cryst. Solids* **2008**, *354*, 3643–3648.
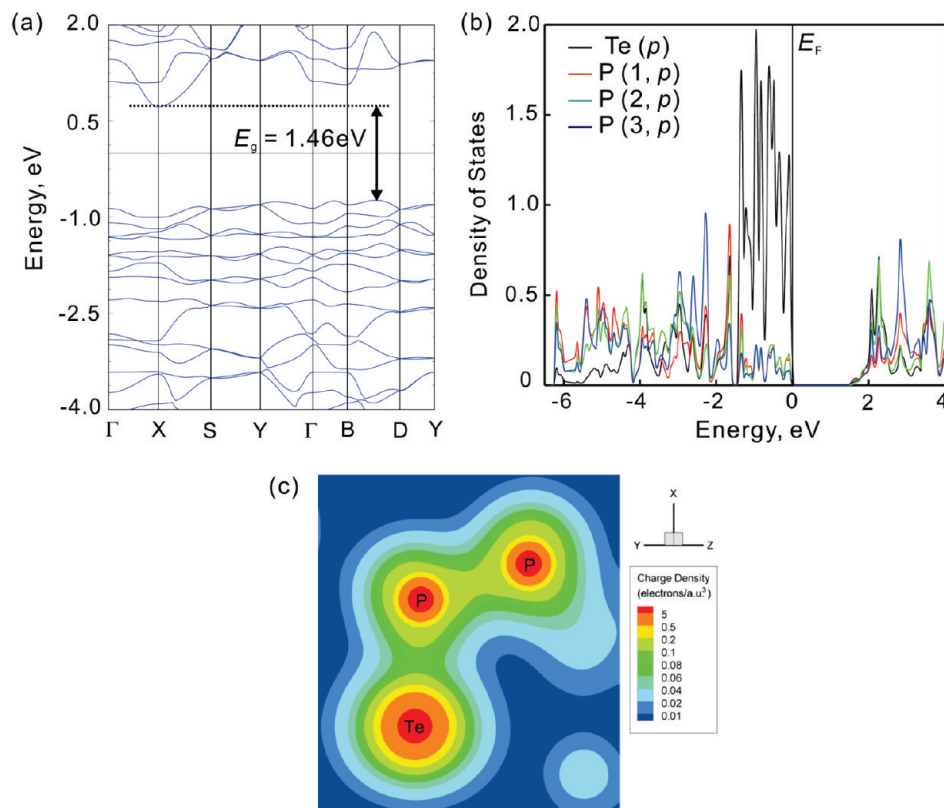
Figure 5. (a) The electronic band structure of $K_4P_8Te_4$. (b) The projected density of states for *p*-orbitals of individual elements (Te and P), and (c) the contour plot of the total charge density of $K_4P_8Te_4$ calculated with the sX-LDA method.

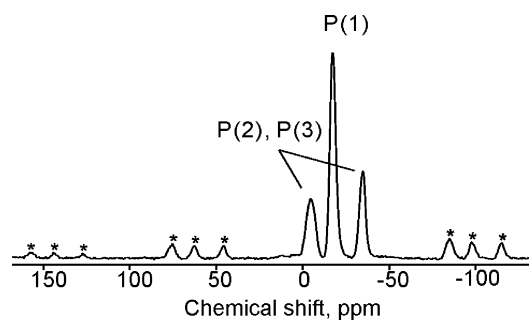**Figure 6.** ^{31}P solid-state MAS NMR spectrum of $K_4P_8Te_4$. The asterisks (∗) denote spinning side bands.

all-covalent networks.[55,56] Although the mechanism of switching from glass to crystalline $K_4P_8Te_4$ is not yet understood, it likely involves the two different types of binding found in the structure, ionic (K···Te) and covalent (P−P and P−Te). Such bonding anisotropy determines glass formation tendency and in principle it could be used to control it.[49,54] Detailed studies are needed to understand how the coexistence of both ionic and covalent bonding affects the phase-change and other physical properties in these materials.

The ^{31}P solid-state magic angle spinning (MAS) NMR spectrum of $K_4P_8Te_4$ revealed three isotropic chemical shifts at −4.3, −16.9, and −34.6 ppm, Figure 6, consistent with the crystallographic analysis. Because the ratio of the integrated intensity is 1.1:2.0:1.0, the peak at −16.9 ppm can be assigned to P(1). The P(1)−P(1) fragment is the shared bond between

the fused cyclohexane chairs of the phosphorus backbone, and has no bonding with Te. The peaks at −4.3 and −34.6 ppm can be attributed to atoms P(2) or P(3). The $\sigma_{33} - \sigma_{11}$ chemical shift anisotropy (CSA) principal value differences were ~188, 116, and 187 ppm, respectively, and also support the assignment. Because P(1) only has homoatomic bonding in contrast to P(2) and P(3) which bond to Te, it can be considered more crystallographically and magnetically symmetric than the others. For selenophosphate anions, the CSA principal value difference correlates inversely with the degree of local symmetry about P.[57] P(2) and P(3) have very similar local geometric environments and could not be individually assigned.

3.3. Electronic Structure Calculations and Bonding. To explore the unusual P−Te bonding in $K_4P_8Te_4$ at a deeper level as well as the nature of the band gap, we performed ab initio density functional calculations with the full-potential linearized augmented plane wave (FLAPW) method.[28]

The electronic structure of $K_4P_8Te_4$ was calculated with the fully first-principles screened-exchange local density functional approximation (sX-LDA) scheme[58,59] and spin−orbit coupling (SOC). The sX-LDA method is known to yield great improvements of the excited electronic states such as band gaps and band dispersion because of its better long-range description of the exchange-correlation hole compared to the local density approximation (LDA). The sX-LDA calculation predicted a band gap of 1.46 eV as shown in Figure 5a, which is close to the experimental band gap at 1.4 eV. The valence band maximum

(55) Varshneya, A. K. *J. Non-Cryst. Solids* **2000**, *273*, 1–7.
(56) Greaves, G. N.; Sen, S. *Adv. Phys.* **2007**, *56*, 1–166.
(57) Canlas, C. G.; Kanatzidis, M. G.; Weliky, D. P. *Inorg. Chem.* **2003**, *42*, 3399–3405.
(58) Asahi, R.; Mannstadt, W.; Freeman, A. J. *Phys. Rev. B* **1999**, *59*, 7486–7492.
(59) Bylander, D. M.; Kleinman, L. *Phys. Rev. B* **1990**, *41*, 7868–7871.

(VBM) occurs along the B−D direction (Figure 4a) while the conduction band minimum (CBM) is located at the X point, which leads to an indirect band gap. The electronic states between −1.5 eV and the VBM in the band structure are less dispersed compared to the lower energy levels, which can be attributed to the localized character of these orbitals, as explained below.

The projected angular-momentum-resolved density of states (DOS) for Te and P p-orbitals are shown in Figure 5b. They show a strong p−p mixing effect, which is very similar to that of BaP_4Te_2.[9] The p−p mixing in $K_4P_8Te_4$ makes for roughly three distinct regions in the DOS for the energy between −6.5 eV and the VBM. The strong contribution of Te p-orbitals to the energy states between −1.5 eV and the VBM are mainly due to the lone-pair states of Te atoms. The small dispersion shown in this energy range of the band structure is caused by these localized lone-pair states. The most interesting energy levels in $K_4P_8Te_4$ are located between −4.2 and −1.5 eV, which derive mainly from P−Te ppσ-bonding. The covalent bonding character between Te and P can also be seen in the contour plots of the total charge density, Figure 5c. The charge densities which are relatively high along the Te−P and P−P bond axes clearly suggest a strong Te−P covalent bonding character. The lower energy levels [at −6.5 eV to −4.2 eV] are mainly composed of P p-orbitals because of the strong covalent interactions in the P−P bonds.

3.4. Nanospheres. An attractive property of $K_4P_8Te_4$ is that it can be brought into hydrazine solution at room temperature. The bonding anisotropy in $K_4P_8Te_4$ and the presence of K ions are reflected in the chemical reactivity in this strongly polar solvent. Apparently, solvation of the K^+ cation by hydrazine overcomes the lattice energy of the solid and leads to the separation from the anionic $[P_8Te_4^{4-}]$ entities, bringing them in solution which amounts to exfoliation. The possibility to exfoliate or even dissolve mineral compounds is of major importance because it creates new possibilities for functionalizing solids and processing them into useful forms by solution chemistry methods.[22,23] It also allows entry into the synthesis of new organic−inorganic hybrids and nanocomposite materials.[60−63] This is known as exfoliation.[64−66]

For example, single crystals of $K_4P_8Te_4$ dissolve in anhydrous N_2H_4 under N_2 atmosphere and with magnetic stirring to produce a deep black/reddish solution. The solution is stable over several months in N_2 atmosphere. The addition of ethanol in a 2 week-aged solution precipitates out the compound, and transmission electron microscopy (TEM) examination showed that the majority of it consists of nanospheres, accompanied by some nanowires as a minor species. High resolution TEM (HRTEM) image of the latter shows lattice fringes aligned along the crystallographic *b**-axis ($[P_8Te_4^{4-}]$ chain direction) and the lateral spacing is uniform at 4.0 Å, which corresponds to the (102) lattice

(60) Davidson, P.; Batail, P.; Gabriel, J. C. P.; Livage, J.; Sanchez, C.; Bourgaux, C. *Prog. Polym. Sci.* **1997**, *22*, 913–936.
(61) Davidson, P.; Gabriel, J. C.; Levelut, A. M.; Batail, P. *Adv. Mater.* **1993**, *5*, 665–668.
(62) Golden, J. H.; Disalvo, F. J.; Frechet, J. M. J. *Chem. Mater.* **1995**, *7*, 232–235.
(63) Hornbostel, M. D.; Hillyard, S.; Silcox, J.; Disalvo, F. J. *Nanotechnology* **1995**, *6*, 87–92.
(64) Davidson, P.; Gabriel, J. C. P. *Curr. Opin. Colloid Interface Sci.* **2005**, *9*, 377–383.
(65) Choy, J. H. *J. Phys. Chem. Solids* **2004**, *65*, 373–383.
(66) Wang, L.; Rocci-Lane, M.; Brazis, P.; Kannewurf, C. R.; Kim, Y. I.; Lee, W.; Choy, J. H.; Kanatzidis, M. G. *J. Am. Chem. Soc.* **2000**, *122*, 6629–6640.
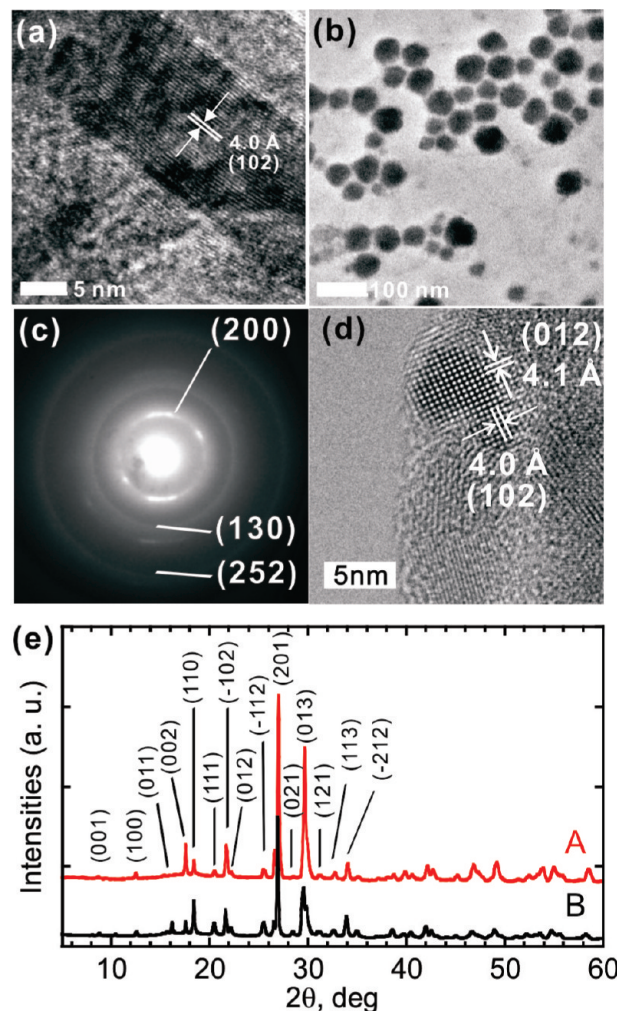

Figure 7. (a) High resolution TEM (HRTEM) image of $K_4P_8Te_4$ chain. The lateral spacing between lattice fringes is 4.0 Å, which corresponds to the (021) lattice plane. (b) TEM image of dispersed $K_4P_8Te_4$ nanosphere. (c) Selected area electron diffraction pattern of $K_4P_8Te_4$ nanospheres with indexing. (d) Lattice image of single $K_4P_8Te_4$ nanosphere, indicative of single crystalline nature. The lattice planes of (012) and (102) are indexed. (e) X-ray powder diffraction patterns of (A) $K_4P_8Te_4$ nanosphere isolated with methanol and (B) pristine bulk $K_4P_8Te_4$ for comparison. Major peaks are indexed.

planes of $K_4P_8Te_4$ (Figure 7a). Energy dispersive microscopic elemental analysis of the sample examined by TEM gave a composition close to $K_4P_8Te_4$, that is, "$K_{4.8}P_8Te_{3.5}$" (Supporting Information S1). The distribution of diameters of nanospheres was ∼10 to 30 nm (Figure 7b). HRTEM image shows the lattice images of a single $K_4P_8Te_4$ nanosphere with reflections indexed to its crystal structure indicating full recovery of the compound by precipitation from solution (Figure 7c).

When exfoliated or dispersed in solution, materials typically generate nano/molecular species that can remain intact or rearrange compared to the corresponding bulk phases. Examples include $KPdPS_4$,[22,23] $LiMo_3Se_3$,[24−27] and $NaNb_2PS_{10}$[67] for 1-D; and MoS_2,[68] WS_2,[69] $K_4Nb_6O_{17}$,[70] and $Bi_4Ti_3O_{12}$[71] for 2-D

(67) Camerel, F.; Gabriel, J. C. P.; Batail, P.; Davidson, P.; Lemaire, B.; Schmutz, M.; Guilk-Krzywicki, T.; Bourgaux, C. *Nano Lett.* **2002**, *2*, 403–407.
(68) Divigalpitiya, W. M. R.; Frindt, R. F.; Morrison, S. R. *Science* **1989**, *246*, 369–371.
(69) Tsai, H. L.; Heising, J.; Schindler, J. L.; Kannewurf, C. R.; Kanatzidis, M. G. *Chem. Mater.* **1997**, *9*, 879–882.

materials. We presume that $K_4P_8Te_4$ in hydrazine behaves similar to $KNiPS_4$[22,23] that exhibited autofragmentation of the exfoliated $[NiPS_4^-]$ chain to the discrete cyclic molecular $[Ni_3P_3S_{12}]^{3-}$ anion in polar organic solvents such as DMF. The nature of the $K_4P_8Te_4$ solutions was studied with solution-state NMR spectroscopy, mass spectrometry and PDF analysis, sections below.

$K_4P_8Te_4$/hydrazine solution is convertible to a crystalline or amorphous solid according to treatment methods. The highly crystalline nanospheres were isolated from $K_4P_8Te_4$/hydrazine solution by precipitation with anhydrous methanol. The X-ray powder diffraction pattern of the precipitated residue matched well with that of a theoretical calculation (Figure 7e). The precipitate is crystalline $K_4P_8Te_4$. The band gap of the recovered $K_4P_8Te_4$ was measured at 1.62 eV, which is significantly blue-shifted from 1.40 eV of the bulk pristine phase which is consistent with the nanosize scale of the compound. However, when the solution was evaporated to dryness by blowing N_2, only a hydrazine-containing sticky amorphous black solid was obtained. TGA of the residue performed at a rate of 2 °C min^{-1} showed that the hydrazine trapped in the structure was removed completely by 250 °C.

3.5. Solution Phase Chemistry of $K_4P_8Te_4$. NMR Spectroscopy and Mass Spectrometry.

To study speciation in solutions of $K_4P_8Te_4$, ^{31}P solution-state NMR spectroscopy (Figure 8) and electrospray ionization (ESI) mass spectrometry (MS) (Figure 9) studies were performed as a function of time: 33 h, 59 h, 156 h, and 1 month after $K_4P_8Te_4$ crystalline powders were dissolved in hydrazine. The two techniques were complementary to each other. Undissolved solid, if any, was filtered before the measurements.

After 33 h, the solution was still almost clear with a slight hazy gray-tint and showed a hint of a broad ^{31}P resonance at ∼ −30 ppm and an MS peak at $m/z = 348.8$, indicative of an early exfoliation stage (see TEM image in Figure 7a). The resonance at δ ca. −30 ppm is possibly assigned to the exfoliated $[P_8Te_4^{4-}]$ chains because of the comparable chemical shift to that of crystalline solid (see Figure 6) and the broad line width. At this stage, the concentration of the dissolved solution was too weak to give a well-defined NMR spectrum. After 59 h, a pale-gray solution gave a sharp singlet peak at 31.6 and 5.0 ppm and an enhanced broad resonance at ca. −32 ppm, coupled with the development of MS peaks at $m/z = 348.8$ for $[KP_8Te_4(N_2H_4)_{7.5}]^{3-}$ and 376.8 for $[KP_8Te_4(N_2H_4)_{10}]^{3-}$. Consistent with the MS data, the isotropic singlet resonances at 31.6 and 5.0 ppm are much sharper than those of the exfoliated chains, and correspond to small molecular $[P_8Te_4]$ species, given by depolymerization/fragmentation of the 1-D chains. The chemical shift at 31.6 ppm, possibly corresponds to P atom bonded to Te atom. This is because Te satellites at 36.4 and 26.6 ppm are observed with one-bond P−Te J coupling constant at 790.5 Hz. The chemical shift at 5.0 ppm is assigned to bridging P atoms with no Te atoms. Note that orthorhombic black phosphorus consists of two-dimensional sheets of six-membered P_6 rings in a chair conformation and show a ^{31}P isotropic resonance at 22.2 ppm.[72] The narrow line width is diagnostic of rapidly tumbling small molecular species. Sharp peaks are dominant in the longer aged solution, suggesting depolymerization appears to be concomitant with dissolution.

Figure 8. Solution-state ^{31}P NMR spectra of $K_4P_8Te_4$ in hydrazine in a time-scale of 33 h, 59 h, 156 h, and 1 month after $K_4P_8Te_4$ solution in N_2H_4 was prepared. The asterisks (∗) denotes one-bond P−Te coupling with $^1J_{P-Te} = 790.5$ Hz. The $[P_8Te_4]^{4-}$ anion is represented from the crystal structure.
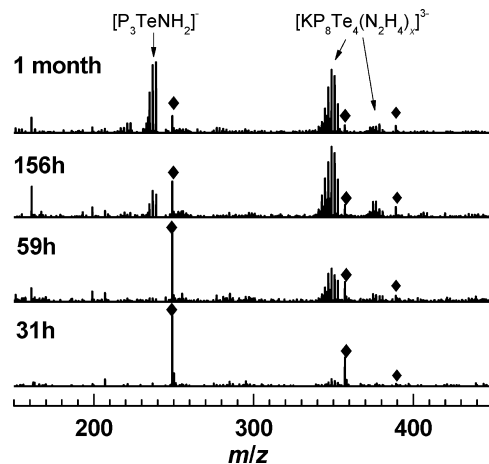
Figure 9. ESI mass spectrometry data from a sample of $K_4P_8Te_4$ dissolved in hydrazine taken over a period of one month; ◆ denotes the artifacts that originate from the blank: $x = 7.5$ for $m/z = 348.8$; $x = 10$ for $m/z = 376.8$.

When aged for 156 h, the solution turned dark black/reddish. The NMR spectrum showed the same sharp peaks at 31.6 and 5.0 ppm, with enhanced resonances at −30, −32, and −34 ppm. MS exhibited increasing peaks at $m/z = 125$ for $[HP_7(N_2H_4)]^{2-}$ and 238.9 for $[P_3TeNH_2]^-$. This is consistent with significant breakdown of the chains. Finally, one month-aged solutions gave prevailing NMR peaks at $\delta = 31.6$ and 5.0 ppm and a well-

(70) Miyamoto, N.; Nakato, T. *Adv. Mater.* **2002**, *14*, 1267–1270.
(71) Kim, J. Y.; Chung, I.; Choy, J. H.; Park, G. S. *Chem. Mater.* **2001**, *13*, 2759–2761.
(72) Lange, S.; Schmidt, P.; Nilges, T. *Inorg. Chem.* **2007**, *46*, 4028–4035.
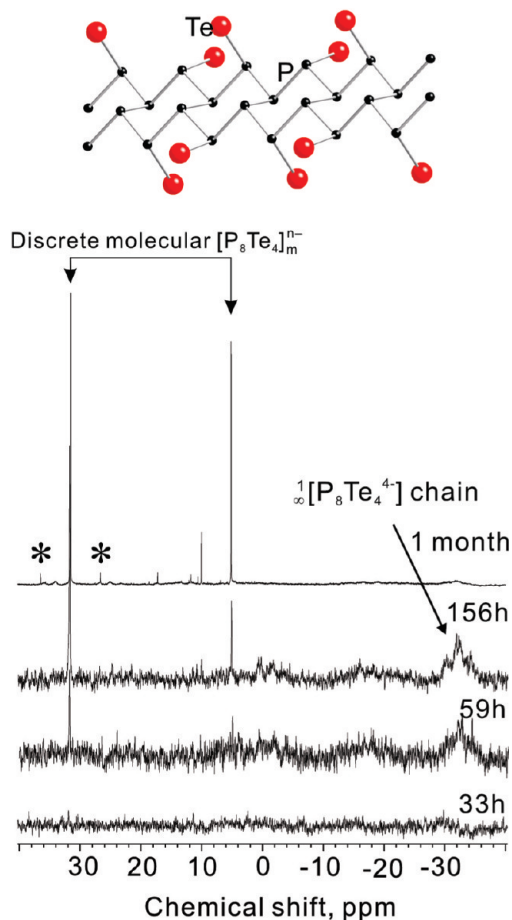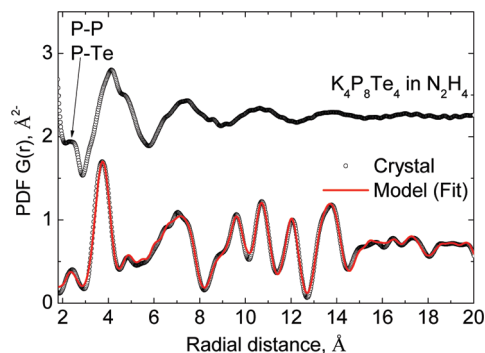
Figure 10. (Top) Experimental pair distribution function $G(r)$ of a 2 week aged solution; (bottom) $G(r)$ of crystalline $K_4P_8Te_4$. The calculated PDF using the crystallographic coordinates is shown as the red line.
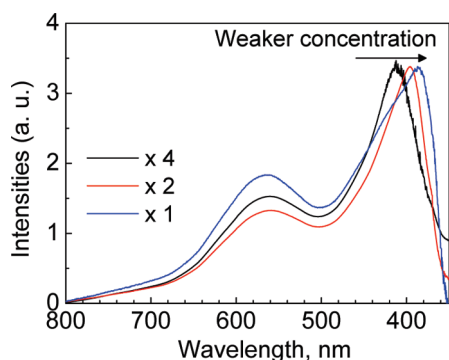

Figure 11. Normalized UV absorbance spectra with respect to the variable concentration of dissolved $K_4P_8Te_4$ in hydrazine. The solution was successively diluted by 50% from I to II to III.

resolved minor peak at $\delta = 10.1$ ppm. At this stage, resonances around ca. -32 ppm are very weak. The resonance at 10.1 ppm is related to further fragmented molecular species from $[P_8Te_4]$.

The above observations are consistent with the TEM results and suggest that $K_4P_8Te_4$ in hydrazine is exfoliated to give the polymeric chain of $[P_8Te_4{}^{4-}]$, followed by further depolymerization/fragmentation to smaller molecular P/Te species. Even longer exposure to hydrazine, as shown in aged solutions, appears to further breakdown these molecular species.

Solution Phase PDF Analysis. An atomic PDF analysis of a 2 week-aged $K_4P_8Te_4$ solution supports the above discussion on the dissolution process. The experimental PDF of the solution shows well-defined correlations only up to $\sim$15 Å, indicative of a well-defined local structure, Figure 10. The PDF of the solution samples is different from that of the glass which shows greater similarity to the local structure of the crystalline form. Only the first correlation at 2.4 Å of the solution PDF is close to that of the crystalline phase, which corresponds to P—P and P—Te covalent bond distances. The longer correlations do not match with those of the crystalline phase suggesting a structural rearrangement in solution to give chemical species that still possess P—P and P—Te covalent bonds. This result excludes the possibility of $K_4P_8Te_4$ nanospheres forming during dissolution, instead they likely form during precipitation.

UV—Visible Absorbance and Photoluminescence. The λ_{max} of UV—vis absorbance of $K_4P_8Te_4$ solutions is dramatically blue-shifted ($\sim$3.0 eV) from the band gap value of the bulk crystalline phase at 1.40 eV, Figure 3c and 11. This is consistent with $[P_8Te_4]^{4-}$ anions being separated from one another upon dissolution and their likely rearrangement to a different P/Te species, in agreement with the solution PDF data discussed above.
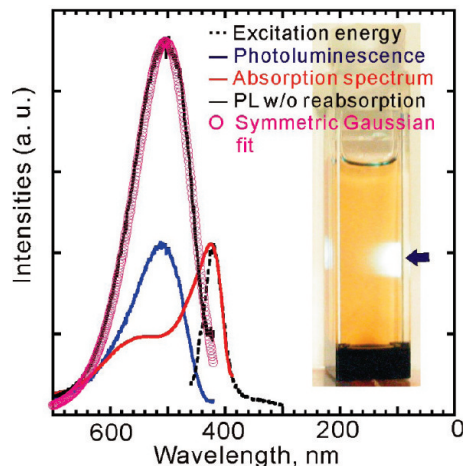

Figure 12. Room-temperature PL (blue line) under excitation at 380 nm (dashed line) and absorption (red line) spectra obtained from $K_4P_8Te_4$/hydrazine. The solid black line corresponds to the predicted PL after correcting the reabsorption effect, superimposed by a symmetric Gaussian fit. The inset exhibits the white emission from $K_4P_8Te_4$/hydrazine solution in a cuvette when 355 nm Nd:YAG laser was introduced at the point marked by an arrow.

Successive dilution of the solution by hydrazine to a half and a quarter concentration shifts the λ_{max} deeper into the UV region, indicative of rearrangement to various molecular species.

The $K_4P_8Te_4$/hydrazine solution exhibited photoluminescence (PL) at room temperature (Figure 12). The PL was independent of solution concentration. It is noteworthy that the PL entirely spans the visible region ($\sim$420 to 690 nm) with unusually large Stokes shift ($\sim$81 nm). When a 355 nm Nd:YAG laser with pulse width of 15 ps was introduced, white light with slight blue-tint was observed (see inset). Statistically, the PL peak should be symmetric, but the observed peak shape is asymmetric owing to reabsorption of the PL. We can approximately reproduce a symmetric peak by multiplying the observed absorption by $\exp[\alpha(E)d]$, where $d \approx 1$ cm is the thickness of a cuvette. As confirmed by the superimposed Gaussian fit, the predicted peak distribution is symmetric around 2.46 eV.

4. Concluding Remarks

$K_4P_8Te_4$ is a new member of the emerging class of phase-change materials that are compositionally stoichiometric and possess alternating ionic and covalent bonding. The synthesis of $K_4P_8Te_4$ exemplifies the suitability of the molten salt method to prepare tellurophosphates that previously had long been elusive. The compound features the unique $[P_8Te_4{}^{4-}]$ chain with low valent P and rare P—Te bonding. The $K_4P_8Te_4$ readily forms various states of crystalline and glassy forms, nanospheres, and dissolution in solution. The glassy phase is easily accessible by melt quenching to room temperature and is switchable to the corresponding crystalline phase by heat treatment. The local structure of the basic building blocks in the glass is similar to those in the crystal which accounts for the facile restoration of the crystal structure from the amorphous phase.

The high solubility of $K_4P_8Te_4$ in hydrazine to give predominantly molecular species, opens up possibilities for new chemistry that could give rise to the synthesis of wide range of metal tellurophosphate compounds via a *chimie deuce* route, functional organic—inorganic hybrids,[73,74] and nanocomposite

(73) Judeinstein, P.; Sanchez, C. *J. Mater. Chem.* **1996**, *6*, 511–525.
(74) Sanchez, C.; Soler-Illia, G.; Ribot, F.; Lalot, T.; Mayer, C. R.; Cabuil, V. *Chem. Mater.* **2001**, *13*, 3061–3083.

formation,[24] gel-formation[75,76] and liquid crystalline behavior.[60] The dissolution process of $K_4P_8Te_4$ appears to be driven by an exfoliation/fragmentation process as supported by ^{31}P NMR spectroscopy, electrospray ionization mass spectrometry, UV−vis absorbance, PDF analysis, and TEM studies. The $K_4P_8Te_4$ solution exhibited highly desirable white emission with slight blue-tint when excited above 3.5 eV. Precipitation from solution results in crystalline $K_4P_8Te_4$ nanospheres with full recovery of the crystal structure. In this regard, precipitation reactions in the presence of different cations are expected to produce new phosphorus tellurides. In addition, the formation of nanospheres suggests that films of $K_4P_8Te_4$ could readily be deposited.

Supporting Information Available: EDS spectrum and elemental mapping of $K_4P_8Te_4$ nanosphere and X-ray crystallographic file in CIF format. These materials are available free of charge via the Internet at http://pubs.acs.org.

JA907273G

(75) Bag, S.; Arachchige, I. U.; Kanatzidis, M. G. *J. Mater. Chem.* **2008**, *18*, 3628–3632.
(76) Bag, S.; Trikalitis, P. N.; Chupas, P. J.; Armatas, G. S.; Kanatzidis, M. G. *Science* **2007**, *317*, 490–493.

The Tellurophosphate $K_4P_8Te_4$: Phase-Change Properties, Exfoliation, and Photoluminescence in Solution

In Chung,[†,‡] *Jung-Hwan Song,*[§] *Myung Gil Kim,*[‡] *Christos D. Malliakas,*[†,‡] *Angela L. Karst,*[†]

Arthur J. Freeman,[§] *David P. Weliky,*[†] *and Mercouri G. Kanatzidis*[†,‡]*

[†]Department of Chemistry, Michigan State University, East Lansing, MI 48824.

[‡]Department of Chemistry, Northwestern University, Evanston, IL 60208.

[§]Department of Physics and Astronomy, Northwestern University, Evanston, IL 60208.

Supporting Information

Contents

Figure S1. The representative EDS spectrum of single $K_4P_8Te_4$ nanosphere.

Figure S2. TEM image and EDS elemental mapping of K, P, and Te atoms.

Figure S1. Representative energy dispersive spectroscopy (EDS) spectrum of single $K_4P_8Te_4$ nanosphere giving a composition of "$K_{4.8}P_8Te_{3.5}$", reasonably close to $K_4P_8Te_4$.
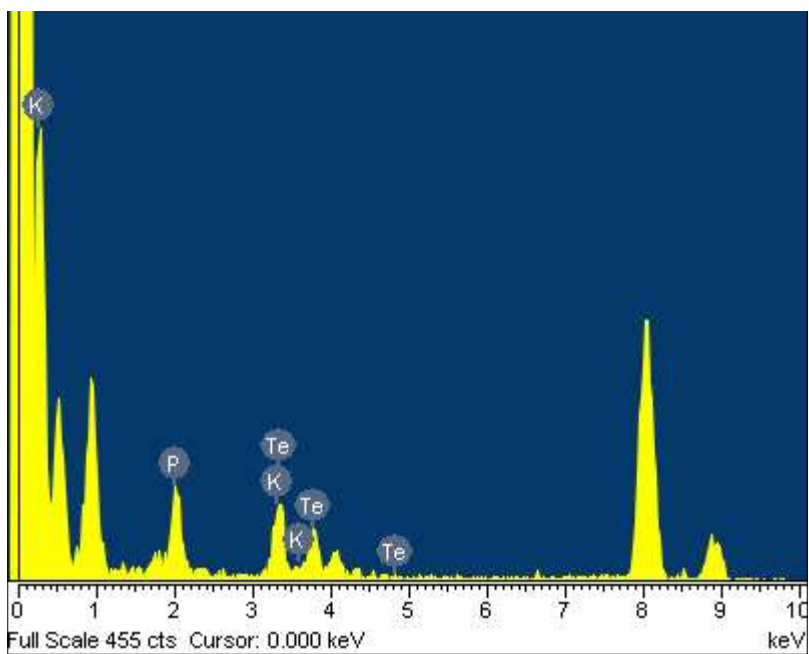
Figure S2. TEM image and EDS elemental mapping of K, P, and Te atoms indicating the existence of all elements on the $K_4P_8Te_4$ nanoparticles.